

Article

Study of a Center Pipe Oscillating Column Wave Energy Converter Combined with a Triboelectric Nanogenerator Device

Yan Huang ^{1,2,3} , Shaohui Yang ^{1,2,3,*}, Jianyu Fan ^{1,2}, Zhichang Du ^{1,2}, Beichen Lin ^{1,2}, Yongqiang Tu ^{1,2}  and Lei Pan ¹

- ¹ College of Marine Equipment and Mechanical Engineering, Jimei University, Xiamen 361021, China; heyetodd@jmu.edu.cn (Y.H.); xdfy1990@126.com (J.F.); 202061000118@jmu.edu.cn (Z.D.); bclin@jmu.edu.cn (B.L.); 202361000149@jmu.edu.cn (Y.T.)
- ² Key Laboratory of Ocean Renewable Energy Equipment of Fujian Province, Xiamen 361021, China
- ³ Key Laboratory of Energy Cleaning Utilization and Development of Fujian Province, Xiamen 361021, China
- * Correspondence: shaohuiyang@jmu.edu.cn; Tel.: +86-180-6451-9096

Abstract: Wave energy is one of the most widely distributed and abundant energies in the ocean, and its conversion technology has been broadly researched. In this paper, a structure that combines a traditional center pipe oscillating water column and a triboelectric nanogenerator is proposed. Firstly, the structural characteristics and geometric parameters of the device are designed. The working process of the device is introduced, the motion equation of the device is established, and the power generation principle of the triboelectric nanogenerator is deduced and analyzed theoretically. Secondly, hydrodynamic modeling and simulation are carried out, the influence of the bottom shape of the main floating body and the structural parameters of the sag plate on the hydrodynamic force of the device is analyzed, and an electric field simulation of the generation process of the friction nanogenerator is carried out. Finally, experiments involving the wave water tank of the proposed device are conducted, including charging the capacitor of the device under different wave conditions and directly lighting the LED lamp. The performance of the proposed device under different wave conditions is discussed. According to the test results, the feasibility of the proposed device for wave energy conversion is confirmed.

Keywords: wave energy converter; oscillation water column; triboelectric nanogenerator; center pipe



Citation: Huang, Y.; Yang, S.; Fan, J.; Du, Z.; Lin, B.; Tu, Y.; Pan, L. Study of a Center Pipe Oscillating Column Wave Energy Converter Combined with a Triboelectric Nanogenerator Device. *J. Mar. Sci. Eng.* **2024**, *12*, 100. <https://doi.org/10.3390/jmse12010100>

Academic Editor: Pietro Scandura

Received: 23 November 2023

Revised: 28 December 2023

Accepted: 28 December 2023

Published: 3 January 2024



Copyright: © 2024 by the authors. Licensee MDPI, Basel, Switzerland. This article is an open access article distributed under the terms and conditions of the Creative Commons Attribution (CC BY) license (<https://creativecommons.org/licenses/by/4.0/>).

1. Introduction

Ocean wave energy is a kind of renewable energy source that refers to the kinetic and potential energy of ocean surface waves generated by atmospheric wind and of sea water gravity. Wave energy has the characteristics of high energy density, wide distribution, and inexhaustibility. The effective development and utilization of wave energy will greatly alleviate the problem of energy shortage. Therefore, wave energy conversion (WEC) technology is highly valued around the world, especially in coastal areas [1,2].

WEC devices generally consist of three energy conversion stages: the energy intake stage captures wave energy, the energy transfer stage converts wave energy into mechanical energy, and the power generation stage converts mechanical energy into electric energy [3–6]. According to the principle of energy capture, it can be classified as a pressure differential, floating structure, overtopping device, etc. In recent years, one typical kind of pressure differential oscillating water column (OWC) has attracted an increasing amount of attention from scholars [7]. Generally, the main body of the OWC consists of a chamber partially immersed in seawater, an air turbine to transform wave energy to mechanical energy, and an electric generator to transform mechanical energy to electricity. The chamber has two openings at the top and bottom of different

sizes, so that the rise and fall of the ocean waves change the gas in chamber to drive the turbine's rotation. Compared with other WECs, the OWC has a significant advantage of simplicity in that the only moving part of its energy conversion mechanism is the rotor of the turbine above the water level, which rotates at a relatively high speed and directly drives conventional generators [8,9]. In the early stage, OWCs were mainly the shore or nearshore type. With the deepening research into WECs and the increasing need for deep-sea development, the offshore OWC has gradually become the main object of research [10–13].

The center pipe spar buoy, Backward Bent Duct Buoy (BBDB), and front bent duct buoy are the three general types of offshore OWC designs. The BBDB was first proposed by Masuda [14] in 1986, as shown in Figure 1a. The device is lightweight and loosely anchored. Under the action of the waves, the water body resonates with the floating buoy, and the wave is completely reflected in the L-shaped backbend pipe. The backward bent duct type has the opening at the back of the float to meet the wave, while the front bent duct type has the opening at the front of the float to meet the wave. A typical front bent duct type device is the “Whale” designed and developed in Japan. A schematic diagram of the device structure is shown in Figure 1b. There are three independent exhaust chambers at the front, and the rear end is connected to the Wells turbine, with a total fixed power of 110 kW [15]. The main difference between the front bent duct and the back bent duct is that the air chamber of the floating ship is different from the wave-facing surface.

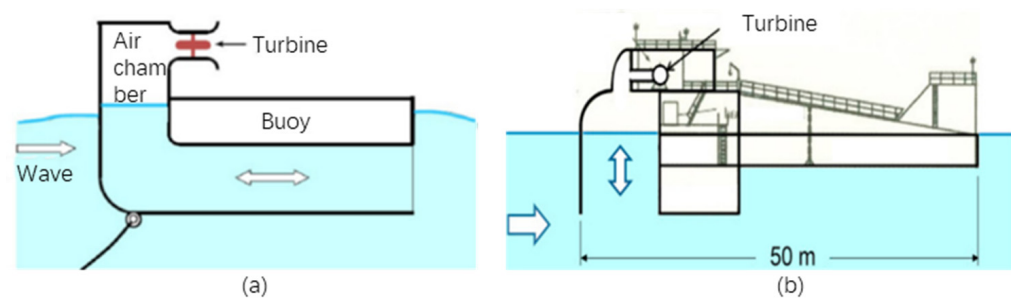


Figure 1. Two typical OWC: (a) Typical BBDB-OWC, (b) Front bent tube “Mighty Whale” OWC.

In 1947, Masuda Shinao [16] invented the first navigation beacon light based on the OWC principle of the center pipe as shown in Figure 2. The center pipe OWC has the advantages of a simple structure, short construction period, and low cost. Currently, the number of practical applications is huge, which has attracted many scholars to invest in the development and utilization of the center pipe wave energy device. Xiao [17] studied buoys with different shapes, e.g., short cone, flat bottom, hemispherical, and long cone. Li [18] and Wu [19] studied the influence of the tailpipe shape on the buoy's hydrodynamic performance. Kim [20] studied the influence of ellipsoidal and cylindrical floating bodies on hydrodynamic coefficients, respectively.

In the process of WEC power generation, it is common to use traditional permanent magnet generators to convert wave energy into electric energy. Alternatively, the triboelectric nanogenerator (TENG) proposed by Wang [21] is capable of converting mechanical energy into electrical energy by combining triboelectrification and electrostatic induction, an approach that has an excellent ability to convert mechanical energy into electrical energy output in low-frequency environments. The triboelectric nanogenerator has the characteristics of high voltage and low current electrical output, and its working mechanism is very suitable for low-frequency micro-vibration wave conditions, especially for the real-time collection and detection of marine information. The implementation of this work requires the use of marine distributed energy self-driven sensing technology, e.g., the triboelectric nanogenerator, which has the advantages of low cost, long endurance, high energy conversion efficiency, and anti-seawater corrosion. Currently, many scholars have studied the combination of triboelectric nanogenerator and wave energy. Lin et al. [22] proposed a triboelectric nanogenerator based on solid–liquid contact for the first time. The prepared TENG consists

of copper as an electrode, graphic pyramid array PDMS, and water. This water-TENG can provide an open circuit voltage of 52 V and a short-circuit current density of 2.45 mA/m², with a peak power density of nearly 0.13 W/m². In 2018, Xu et al. [23] prepared a highly sensitive wave sensor based on the characteristics of liquid–solid interface triboelectric nanogenerators. The research results show that when the electrode width is 10 mm, the output voltage increases linearly with the wave height, and the sensitivity is 23.5 mV/mm. Yang et al. [24] demonstrated the first fully enclosed TENG. TENG was prepared by using a polytetrafluoroethylene (PTFE)–polyamide (PA) film material in a closed sphere. The two TENG units were sealed in a cylinder and were capable of directly lighting up to 60 LED lights under oscillating conditions. Ning et al. [25] reported a frictional nanogenerator with a seagrass imitation structure for collecting wave energy. The output current of a single generator unit was about 10 μA, the voltage was about 260 V, and the maximum power density was 25 μW/m².

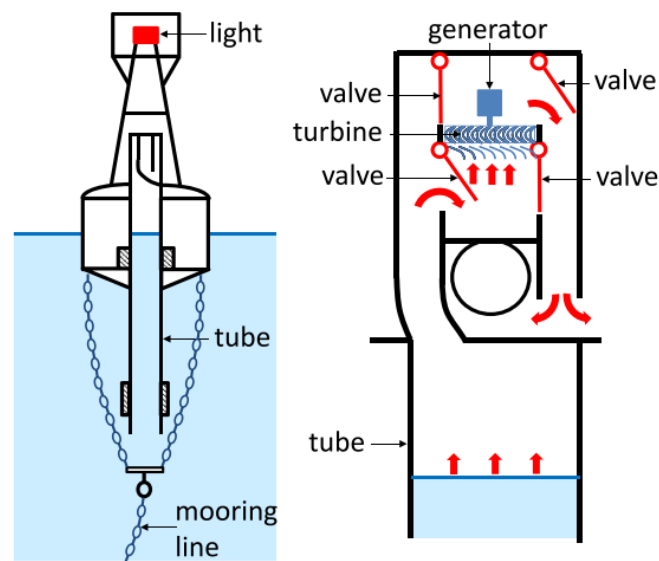


Figure 2. Layout of Masuda's navigation buoy and details of the air flow through the turbine and rectifying valves (The red arrows indicate the air flow).

Until now, various types of triboelectric nanogenerators have been designed to apply in the field of wave energy collection, most of which were based on the characteristics of triboelectric nanogenerators. However, the response optimization of energy capture and energy conversion link in traditional wave energy collection devices is not conducive to the continuous optimization of conversion efficiency. In this paper, a structure combining a central pipe OWC and a triboelectric nanogenerator (CP-TENG) is designed that inherits the traditional OWC structure and exploits the advanced technology of TENG. The designed generator is simple in structure and easy to maintain. The power generation structure of the designed generator has no underwater contact, which provides more possibilities for the application of triboelectric nanogenerator technology in wave energy collection, and provides a certain reference significance for the effective collection of low-frequency wave motion. This paper is organized as follows: In Section 2, the overall idea of the designed structure is introduced; Sections 3 and 4 explain the principle of the designed OWC and TENG separately; Sections 5 and 6 discuss the simulation results of the proposed CP-TENG device; and the water tank test of the proposed CP-TENG is conducted and the relevant results are discussed in the final section.

2. Overall Structure Design of the CP-TENG

A structural construction diagram of the center pipe OWC is shown in Figure 3. The proposed device consists of a main floating body, a heave plate, an impact air turbine, and a disc triboelectric nanogenerator. The floating body mainly provides the overall

buoyancy of the device. The function of the heave plate is to reduce the overall large movement and improve the additional mass of the device. The impact air turbine absorbs the aerodynamic energy of wave conversion to drive the disc triboelectric nanogenerator to convert mechanical energy to electricity.

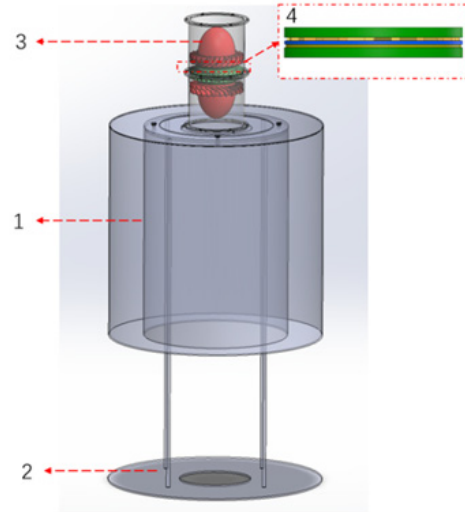


Figure 3. Structure of the central pipe wave energy device (1: floating body, 2: heave plate, 3: impact air turbine, 4: disc triboelectric nanogenerator).

The working process of the CP-TENG is shown in Figure 4. The device floats on the ocean surface and the top of the air chamber is connected to atmospheric pressure. Triboelectric nanogenerators are embedded on both sides of the moving blade and the side of the guide blade near the moving blade. Under the action of waves, the heave of the device affects the liquid level of the central pipe chamber inside the floating body, causing the variation in the air volume in the chamber. When the liquid level in the chamber rises and falls, the volume of the gas in the cavity becomes smaller and greater. Meanwhile, the compression and expansion of air generates reciprocating air flow in the center pipe. The reciprocating air flow drives the moving blade of turbine at a certain angle under the guidance of the guide blades. The guide blades collect both the upward and downward air flow directions and the moving blade drives the turbine in one direction. Then, with the rotation of the moving blade, the triboelectric nanogenerators generate electricity because of the triboelectrification and electrostatic induction.

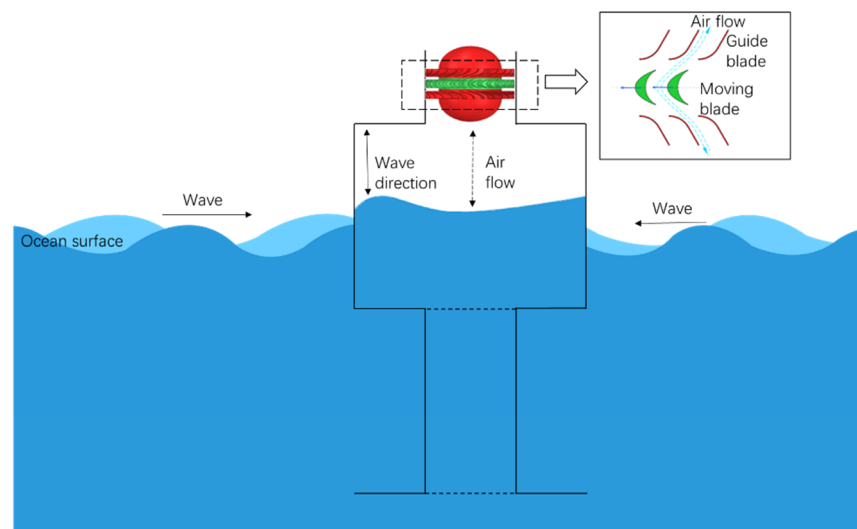


Figure 4. Working principle diagram of the center pipe-type wave energy triboelectric nanogenerator.

3. Hydrodynamics Principle of Floating Body

Assuming that the fluid is an ideal fluid of irrotation and incompressibility, the floating body can be simplified into a cylindrical model with equal diameter. The bottom of the device is a pendant plate, and only the pendant motion is beneficial to the power generation of the center pipe WEC. Other degrees of freedom have limited influence on the energy conversion performance of the power generation system of the center pipe WEC. In order to simplify the calculation, the pendant motion of the center pipe wave energy generator is mainly considered.

Under the action of linear wave load, the dynamic equation of the device can be expressed as

$$[M_{ij} + \Delta M]\ddot{\zeta}_i + [B_{rad} + B_{vis}]\dot{\zeta}_i + [K_{sw} + K_m]\zeta_i = [F_i], \tag{1}$$

where ζ_i is the six-degrees-of-freedom motion amplitude of the floating body, and M is the device mass matrix expressed as

$$M_{ij} = \begin{bmatrix} M & 0 & 0 & 0 & Mz_G & -My_G \\ 0 & M & 0 & -Mz_G & 0 & Mx_G \\ 0 & 0 & M & My_G & -Mx_G & 0 \\ 0 & -Mz_G & My_G & I_{xx} & I_{xy} & I_{xz} \\ Mz_G & 0 & -Mx_G & I_{yx} & I_{yy} & I_{yz} \\ -My_G & Mx_G & 0 & I_{zx} & I_{zy} & I_{zz} \end{bmatrix}, \tag{2}$$

where M is the mass of the device, (Z_G, Y_G, X_G) indicates the centre-of-gravity position of each coordinate axis, I_{ij} indicates the inertial mass.

ΔM is the device additional mass matrix; B_{rad} is the radiation damping matrix; B_{vis} is the viscous damping matrix; K_{sw} is the hydrostatic stiffness; K_m is the mooring stiffness; and F_i is the wave excitation force acting on the device.

The inherent period expression of the free motion of the device is

$$T_i = 2\pi\sqrt{\frac{M_{ii} + \Delta M_{ii}}{K_{ii,sw} + K_{ii,m}}}, \tag{3}$$

where M_{ii} is the device mass matrix and K_{ii} is the stiffness matrix.

The research object of this paper can be simplified as a cylinder, the structure of which has symmetry. For the center pipe wave energy generation device, only the dangling motion is beneficial to its energy conversion, without considering the influence of other degrees of freedom on energy conversion. Equation (3) can be simplified as

$$[M_{ij} + \Delta M_{33}]\ddot{z} + [B_{rad} + B_{33}]\dot{z} + [K_{sw} + K_m]z = [F_z], \tag{4}$$

where ΔM_{33} is the additional mass of the device heave and B_{33} is the device heave damping coefficient. Equation (4) represents the motion equation of the droop of the center pipe wave power generation device under the action of linear waves.

Air turbine is an important part of energy conversion in CP-TENG. By arranging a set of fixed guide blades on both sides of the moving blades, the air flow through the fixed guide blades in the pipeline can drive the moving blades to rotate in the same direction.

As shown in Figure 5, the wave heave in the center pipe of diameter D_1 causes the gas in the chamber to be squeezed into the center pipe of diameter D_2 at the speed v_1 , and then moves to the impact air turbine at the speed v_2 , thus driving the turbine to rotate, assuming that the air flow in the pipe is continuous, non-viscous, and incompressible. The latter assumption is relatively reasonable at these small scales since the volume of the air chamber is much smaller than what would be required to simulate the compressibility effects occurring at full scale [26,27]. The stepped interface in the pipe can be satisfied:

$$\frac{\pi D_1^2 dl_1}{4} = \frac{\pi D_2^2 dl_2}{4}, \tag{5}$$

where dl denotes the instantaneous change in the axial displacement of the gas in the pipe at the interface.

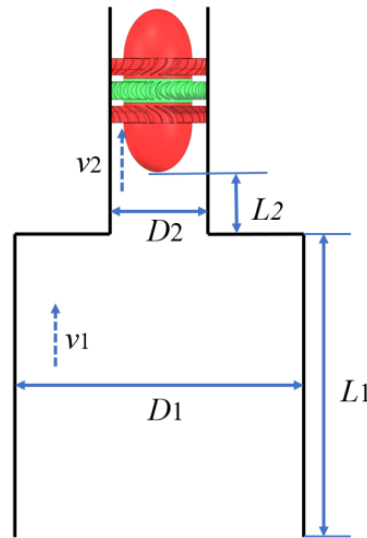


Figure 5. Schematic diagram of the stepped pipe diameter in the center pipe.

We take the derivative of the above equation with respect to time t :

$$\frac{dv_2}{dv_1} = \frac{D_1^2}{D_2^2} \tag{6}$$

where dv denotes the amount of instantaneous change in the axial velocity of the gas in the pipe at the interface. When the bottom diameter of the center pipe is larger than the top diameter, the airflow can be increased to better drive the rotation of the impact triboelectric nanogenerator.

4. Power Generation Principle of Triboelectric Nanogenerator

The working principle of the triboelectric nanogenerator is shown in Figure 6. The rotor electrode slides between Electrode 1 and Electrode 2. At the beginning, the surface of the rotor electrode is in direct contact with the surface of the dielectric material. Due to the difference in triboelectrification and the ability of materials to gain and lose electrons, the rotor electrode surface generates a positive charge, while the dielectric material surface generates negative charges. During the rotation, a potential difference is generated between Electrode 1 and Electrode 2, resulting in a reverse current until the final state. As the electrodes continue to rotate, an alternating current forms in the circuit.

Since thickness d of the dielectric material is much smaller than its width, the metal electrode can be regarded as an infinite parallel plate capacitance, and the influence of its edge effect is ignored through model simplification. The width of the thin slit between Electrode 1 and Electrode 2 is ignored. Under the open circuit condition, assuming that the angle of a single sector electrode is a , the rotation angle of the rotor along the electrode is $a_1 (0 \leq a_1 \leq a)$, the charge density evenly distributed on the surface of the separation area between the rotor electrode and electrode 1 is $-\sigma$, and the open circuit voltage between Electrode 1 and Electrode 2 is V , it can be deduced that when the rotor is aligned with Electrodes 1 or 2, the open circuit voltage in the initial state is

$$V_{1,2} = \frac{2d\sigma}{\epsilon_0\epsilon_r} \tag{7}$$

where ϵ_0 is the vacuum permittivity and ϵ_r is the relative permittivity of the dielectric material.

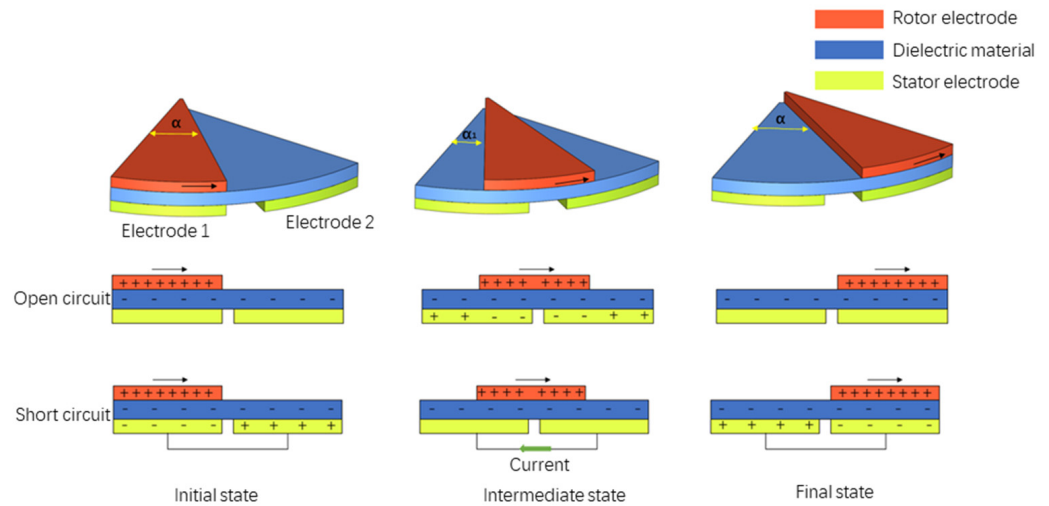


Figure 6. Schematic diagram of the working principle of IW–TENG.

The maximum voltage in a cycle is

$$V_E = \frac{4d\sigma}{\epsilon_0\epsilon_r}. \tag{8}$$

When the rotor is not overlapping with Electrodes 1 and 2, for the charge density of the region where the rotor is not overlapping with the parts of Electrodes 1 and 2,

$$\rho = \sigma. \tag{9}$$

For the area where the rotor overlaps with Electrode 1,

$$\rho_1 = -\frac{\sigma a_1}{a - a_1}. \tag{10}$$

For the area where the rotor overlaps with Electrode 2,

$$\rho_2 = -\frac{\sigma(a - a_1)}{a}. \tag{11}$$

According to Gauss theorem and the charge density distribution, the electric field strength of the dielectric material in the overlapping area of the rotor and electrode can be obtained:

$$E_1 = -\frac{\sigma a_1}{\epsilon_0\epsilon_{r1}(a - a_1)}, \tag{12}$$

$$E_2 = -\frac{\sigma(a - a_1)}{\epsilon_0\epsilon_{r2}a_1}. \tag{13}$$

The open circuit voltage can be calculated:

$$V_{oc} = E_1d - E_2d = \frac{d\sigma(a - a_1)}{\epsilon_0\epsilon_{r2}a_1} - \frac{d\sigma a_1}{\epsilon_0\epsilon_{r1}(a - a_1)}, \tag{14}$$

where E_1 and E_2 are, separately, the electric field strength of the dielectric material in the area where the rotor overlaps with the electrode. When Electrode 1 and Electrode 2 use the same dielectric material, the open circuit voltage can be simplified as

$$V_{oc} = E_1d - E_2d = \frac{d\sigma}{\epsilon_0\epsilon_r} \left(\frac{a - a_1}{a_1} - \frac{a_1}{a - a_1} \right). \tag{15}$$

The short-circuit current I_{sc} relies on the rotational motion velocity of the rotor electrode which is formulated as

$$I_{sc} = \frac{dQ}{dt} = \frac{dQ}{dx} \cdot \frac{dx}{dt} = \sigma \cdot v_r, \tag{16}$$

where v_r denotes the rotation speed of rotor electrode. And the average power is calculated using following equation:

$$P_{ave} = \frac{\int_0^T V \cdot I}{T}, \tag{17}$$

where T is the rotation period of the rotor electrode.

5. Analysis of Hydrodynamic Characteristics for Model Selection of OWC

The device operates under six degrees of freedom of rolling, pitching, yawing, surging, swaying, and heaving, of which heave is an important consideration. The hydrodynamic analysis of the device focuses on the performance index of the buoy in the direction of heave. The frequency domain simulation analysis and hydrodynamic coefficients, such as the damping coefficient, additional mass, and RAO coefficient, are analyzed. The wave frequency in the coastal waters of Fujian Province is generally 0.5~2.5 rad/s. In the hydrodynamics simulation, the change trend of the device in the frequency range of the wave main energy is mainly observed.

5.1. Influence of the Bottom Shape of the Main Floating Body on the Hydrodynamic Force of the Device

Through the structural design of the device, the relationship between the hydrodynamic performance of the device and the bottom shape of the main floating body is analyzed. It is necessary to ensure that the diameter and mass of the device remain unchanged. According to the design requirements, the five devices have an identical mass of 36.65 kg and a diameter of 0.6 m. Model 1 is a cylinder. Models 2 and 3 are circular tables with different bottom diameters. Models 4 and 5 are fillet corners with different bottom diameters. Table 1 lists the specific physical parameters.

Table 1. Physical parameters of Models 1–5.

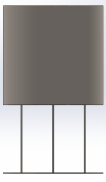
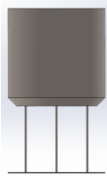
	Model 1	Model 2	Model 3	Model 4	Model 5
Float Shape					
Diameter of bottom (m)	0.6	0.6/0.5	0.6/0.4	0.6/0.5	0.6/0.4
Rotational inertia (I_{xx})	2.54	2.49	2.41	2.52	2.47
Rotational inertia (I_{yy})	2.54	2.49	2.41	2.52	2.47
Rotational inertia (I_{zz})	2.36	2.34	2.33	2.35	2.34

Figure 7 shows the relationship between the hydrodynamic dynamics of different main floating body bottom shapes and the wave frequency. It can be seen from the wave exciting force curve that the main floating body with the bottom shape of a rounded corner has the largest vertical exciting force, in which the vertical exciting force of Model 5 is greater than that of Model 4, and the vertical exciting force of the cylindrical main floating body is the least. It can be seen from the heave damping curve that the heave damping of these bottom shapes is similar, where the heave damping of Model 3 is the largest and that of Model 5 is the smallest. It can be seen from the heave add-on mass curve that the heave add-on mass effect of Model 1 is better than that of the other models. It can be seen from the sag RAO that the sag RAOs of the five models are close to each other at 0~3 rad/s, and

the sag RAO of Model 1 is better than the other four models at 3~4 rad/s. Among the five models, the main floating body of Model 1 is the cylinder at the bottom, which can obtain a better heave response in low-frequency waters.

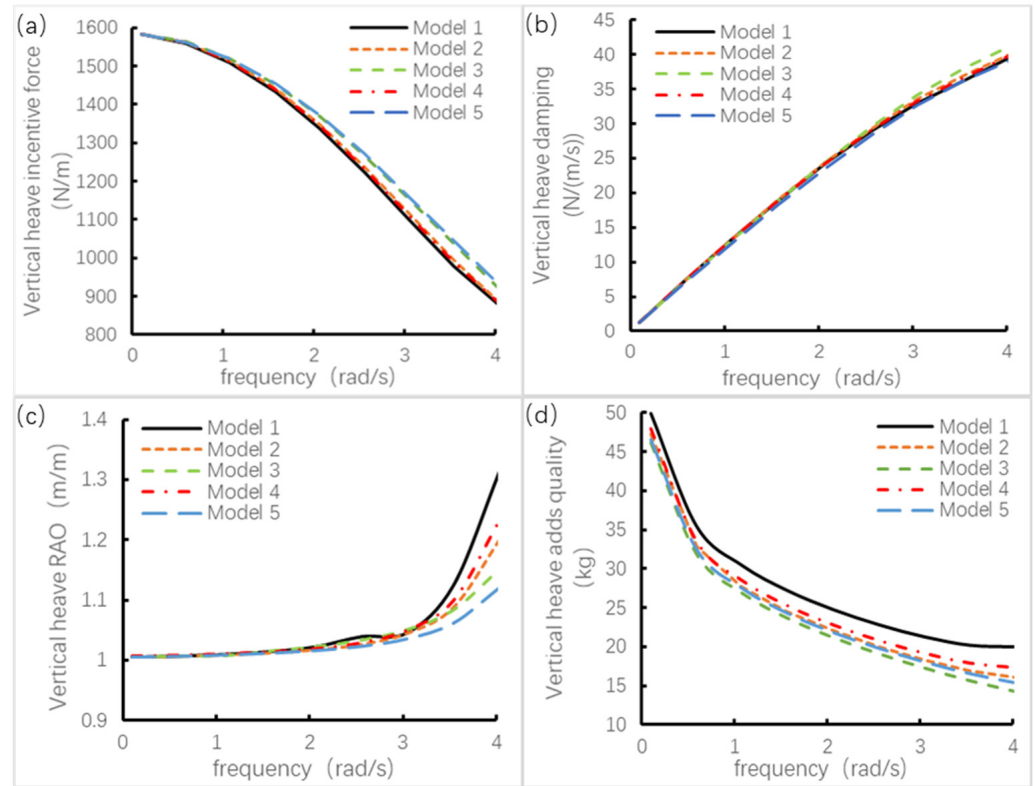
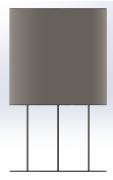


Figure 7. Hydrodynamics curves of the bottom shapes of different main floating bodies changing with wave frequency: (a) heave exciting force curve, (b) heave damping coefficient curve, (c) heave additional mass curve, and (d) heave RAO curve.

5.2. Influence of the Width of the Heave Plate on the Hydrodynamic Force of the Device

When analyzing the influence of heave plate width on the hydrodynamic performance of the device, Model 1, with its better hydrodynamic effect of the bottom shape of the main floating body, was selected as the analysis object. Models 6–9 were established by changing the heave plate width while keeping the shape of the main floating body unchanged. The detailed physical parameters of the model are listed in Table 2.

Table 2. Physical parameters of Models 1 and 6–9.

	Model 6	Model 7	Model 1	Model 8	Model 9
Float Shape					
Swing board width (mm)	400	500	600	700	800
Mass (kg)	33.53	34.93	36.65	38.66	40.99
Rotational inertia I_{xx} (kg·m ²)	2.27	2.48	2.54	3.08	3.49
Rotational inertia I_{yy} (kg·m ²)	2.27	2.48	2.54	3.08	3.49
Rotational inertia I_{zz} (kg·m ²)	2.15	2.24	2.36	2.49	2.68

When the shape of the main floating body is unchanged and the height of the swinging plate is the same, the hydrodynamics of the swinging plate with different widths varies with the wave frequency, as shown in Figure 8. It can be seen from the heave exciting force diagram that the heave exciting force of this model group tends to be the same. It can be seen from the sag damping coefficient curve that when the wave frequency is 0~4 rad/s, and the sag damping of Model 7 is the least, followed by that of Model 6. By contrast, Models 1, 8, and 9, whose sag plate is greater than or equal to the floating body diameter, have similar sag damping. It can be seen from the sag additional mass curve that the sag additional mass of Model 7 decreases more slowly with the increase in wave frequency, and there is no significant difference between Model 7 and the other models. It can be seen from the heave RAO curve that, in this group of models, the influence of the heave plate width change on heave RAO mainly occurs at a wave frequency of 2~4 rad/s. The heave RAOs of Models 1 and 6 are approximately different, and Model 7 has the best effect. In other words, the optimal sag motion response can be obtained at the wave frequency of 2~4 rad/s by reasonably designing the appropriate width of the sag plate.

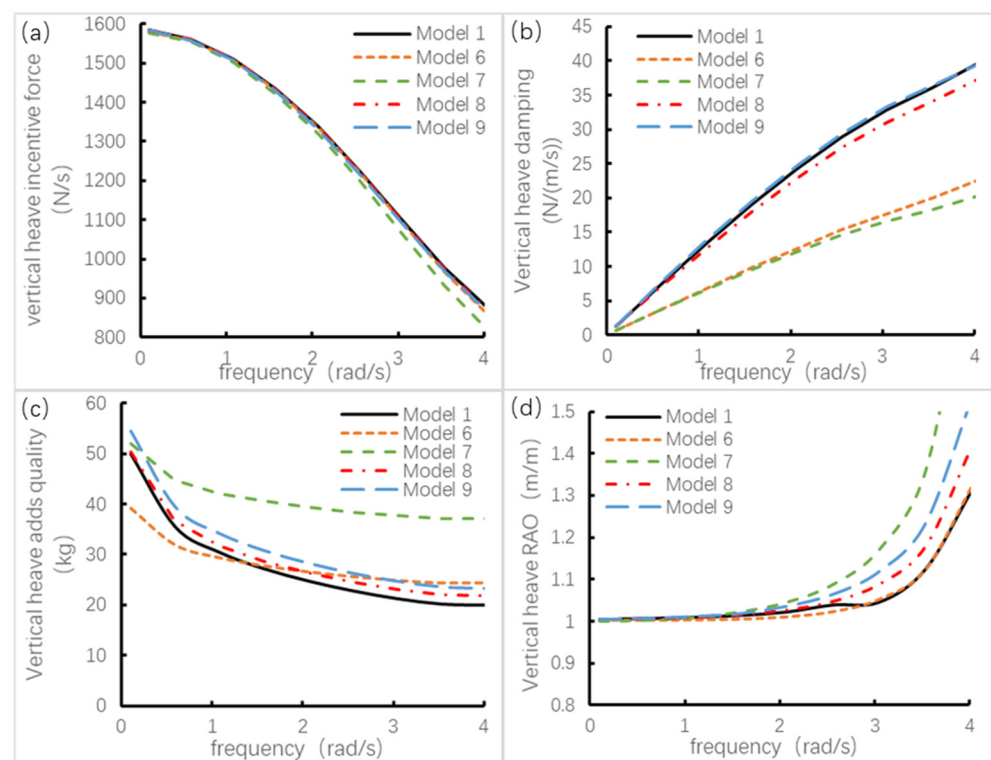


Figure 8. Hydrodynamics curve of different heave plate diameters with wave frequency: (a) heave exciting force curve, (b) heave damping coefficient curve, (c) heave additional mass curve, and (d) heave RAO curve.

6. Electric Field Simulation Analysis for Material Selection of TENG

According to principle in Section 4, the influencing factors of TENG are the thickness and the surface charge density of the dielectric material. This means that the material selection of TENG depends on, on the one hand, the relative dielectric constant of the material, and on the other hand the appropriate balance between thickness and surface charge density in the same material.

In order to verify the influence of different dielectric material thicknesses on the electric potential size, three groups of dielectric film material PTFE with different thicknesses were set on the basis of electric field simulation, which were 0.05 mm, 0.08 mm, and 0.1 mm, respectively. The other setting parameters remained unchanged except for the position changes. In addition, according to the Equations (15) and (16), both voltage and current

are directly proportional to the surface charge density, therefore the simulation results of voltage are only shown for brevity.

Firstly, the potential change trend of a single thickness of PTFE was analyzed: the potential change trend diagram of the rotor electrode is shown in Figure 9a. When the initial state is aligned with bottom Electrode 1, the potential is higher. In the process of moving towards bottom Electrode 2, the potential gradually becomes smaller, reaching the minimum value in the middle position. Subsequently, during alignment with bottom Electrode 2, the potential continually returns to a higher value. Electrode 1 at the bottom continues to decline from a higher value positive potential to 0 V in the middle and then to negative potential, as shown in Figure 9b. The change trend of Electrode 2 at the bottom is opposite to that of Electrode 1 at the bottom, as shown in Figure 10a. For PTFE with increased thickness, it can be found from the three figures that the thinner PTFE makes the electrode potential change more. This is because the thinner the PTFE, the larger the surface charge density. As the triboelectric nanogenerator is contact friction, dielectric materials produce friction and wear in the process of power generation. Thin dielectric materials are more likely to be damaged, resulting in limited power generation performance. In order to ensure the durability of dielectric materials under a certain thickness, this part of the performance test is verified in the fourth part of the experiment.

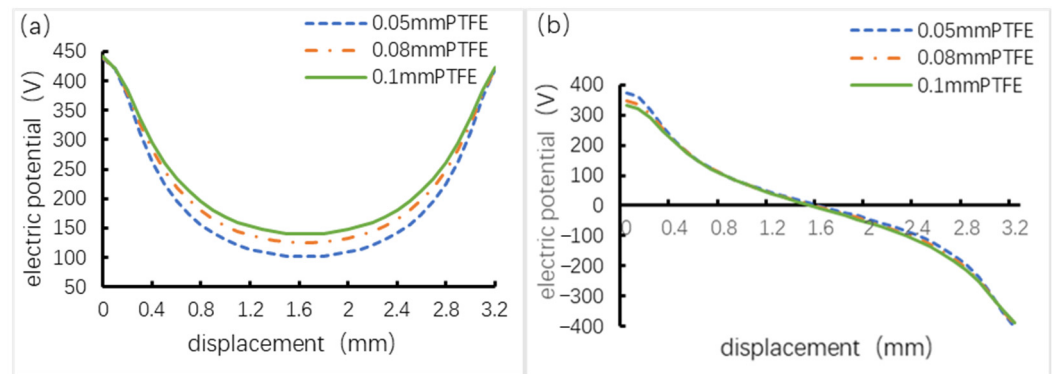


Figure 9. (a) Different thicknesses of PTFE rotor electrode potential trend and (b) different thicknesses of PTFE Electrode 1 potential trend.

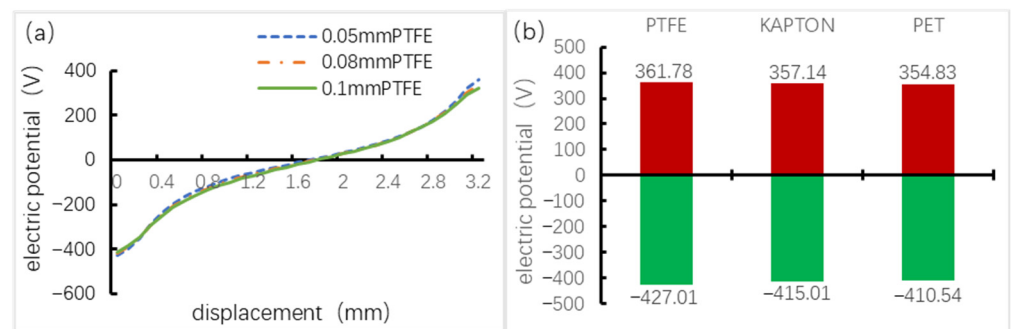


Figure 10. (a) Variation trend of potential of PTFE Electrode 2 with different thicknesses and (b) comparison of peak potential of Electrode 1 with different dielectric materials of 0.05 mm.

Furthermore, the condition of dielectric material thickness of 0.05 mm was simulated, and the potential size diagram of three common dielectric materials, including polytetrafluoroethylene (PTFE), polyimide (Kapton), and polyethylene terephthalate (PET), was compared under this condition, as shown in Figure 10b. It can be seen from the figure that PTFE has the largest peak potential. PET has the smallest peak potential.

7. Prototype Development and Test Environment

Figure 11 shows a two-dimensional assembly diagram of the wave-making flume prototype of the center pipe wave energy triboelectric nanogenerator. Table 3 lists the specific parameters of the model. In addition to the impact triboelectric nanogenerator, the whole device is manufactured and welded in a non-standard metal processing factory. Due to the limited amount of practical engineering experience, in order to highlight the test effect and verify the realizability of the small sensor energy supply of the center pipe wave energy triboelectric nanogenerator, the whole device was scaled to the turbine width of 100 mm based on the original turbine design standards, and a new turbine was 3D printed and assembled.



Figure 11. Physical picture of the center pipe wave energy triboelectric nanogenerator.

Table 3. Model parameters.

Parameter Names	Model
Total height of device, H (m)	1.018
Maximum diameter of float, D (m)	0.6
Main float height, L1 (m)	0.6
Central pipe diameter, D1 (m)	0.4
Maximum diameter of top air port, D2 (m)	0.175
Wall thickness, T1, T2 (m)	0.003, 0.005
Heave plate thickness, T (m)	0.005
Swing board height, L2 (m)	1.01
Sag board connection rod diameter, D3 (m)	0.01
Diameter of the center through hole of the swing plate, D4 (m)	0.2

7.1. Experimentation

The test environment for the prototype is a wave-making flume with a length of 12.5 m, a width of 1.5 m, and a height of 1.2 m (minimum working water depth 0.2 m, maximum working water depth 1.0 m). The test environment is shown in Figure 12. The nanogenerator data acquisition instrument is a Keithley 6514 electrometer, and the electrical output data are saved in real time via the upper computer software, which can satisfy the measurement of experimental data well.



Figure 12. Test environment of the wave-making tank.

The flume prototype was placed in the back part of the flume throughout the test. The water level of the flume was set to 70 cm. A thin cable was used as the anchor at the bottom of the prototype, and the anchor was used as the slack mooring to tie the weight to the other end of the cable. The state of the device in still water and in waves is shown in Figure 13. The electrical output performance test of the device is tested by setting four groups of different cycles and four groups of different significant wave heights, as shown in Table 4. The random wave condition is generated by the JONSWAP spectrum, which has the highest practical usage in ocean engineering studies [28], with significant wave height as 0.12 m and Gama value as one. The application of small electronic components and the electrical output performance under a group of random wave conditions are tested.



Figure 13. State of the prototype in still water and in waves.

Table 4. Parameters of wave height and period under regular waves.

Significant Wave height (m)	0.09	0.12	0.15	0.18
Period (s)	2	2.5	3	3.5

7.2. Test and Result Analysis

(1) Test and analysis of electrical output performance under regular waves

The electrical performance output of the central pipe wave power generation device with different significant wave heights when the wave period is 2 s is shown in Figures 14 and 15. It can be seen from the figure that when the significant wave height is 0.12 m, the electrical performance output of the device is the best, the average open circuit voltage is about 28 V, and the short-circuit current is about 0.56 μ A. In the case of this period, when the significant wave height is higher than 0.12 m, the device shakes violently, and the turbine assembly process and other factors increase the blade clearance under vibration conditions. The blade stalls and exhibits other problems, showing irregularity.

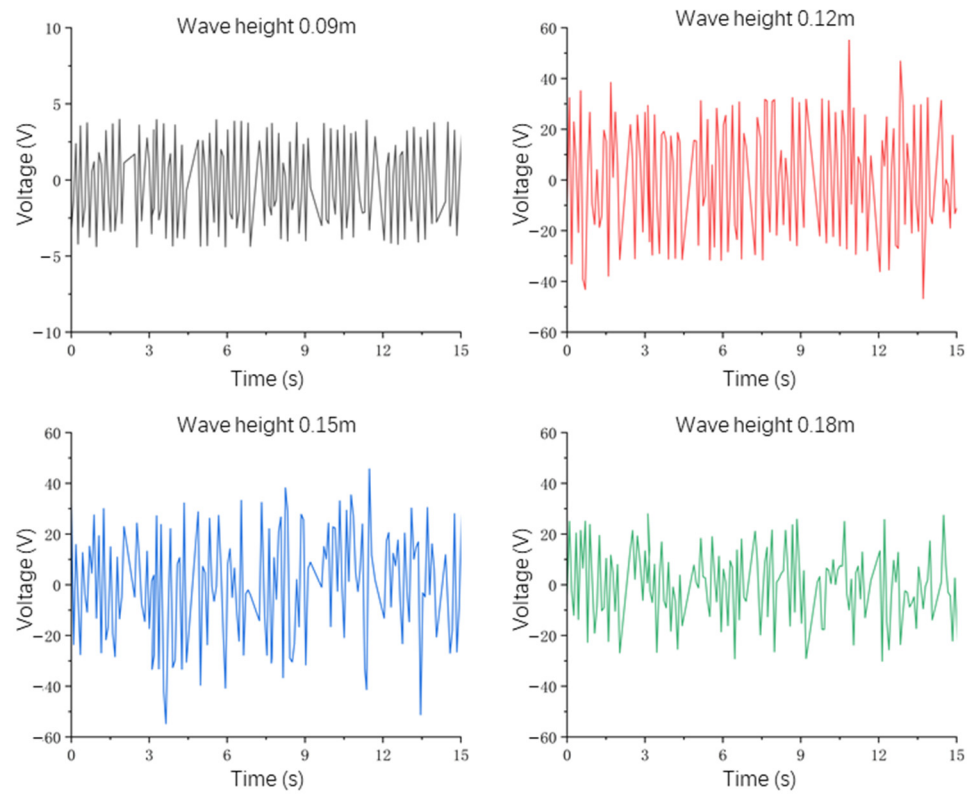


Figure 14. When the wave period is 2 s, the open-circuit voltage output of center pipe wave power converter in different significant wave heights.

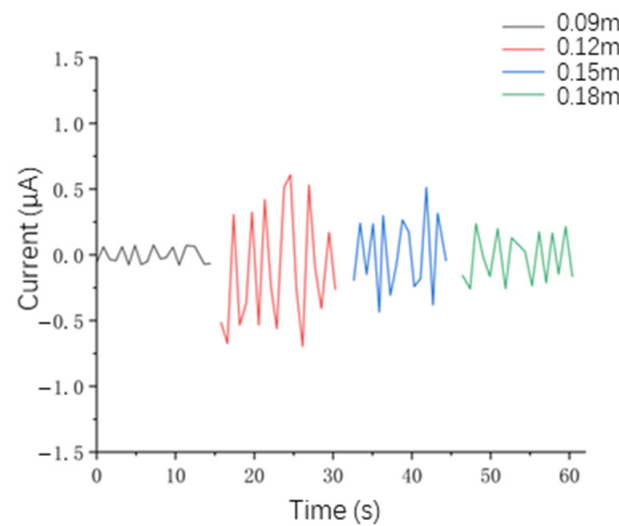


Figure 15. When the wave period is 2 s, the short-circuit voltage output of center pipe wave power converter in different significant wave heights.

The electrical performance output of the center pipe wave power generation device at different wave levels when the wave period is 2.5 s is shown in Figures 16 and 17. It can be seen from the figure that when the significant wave height is 0.12 m, the electrical performance output of the device is the best, the open circuit voltage is about 24 V, and the short-circuit current is about 0.38 µA.

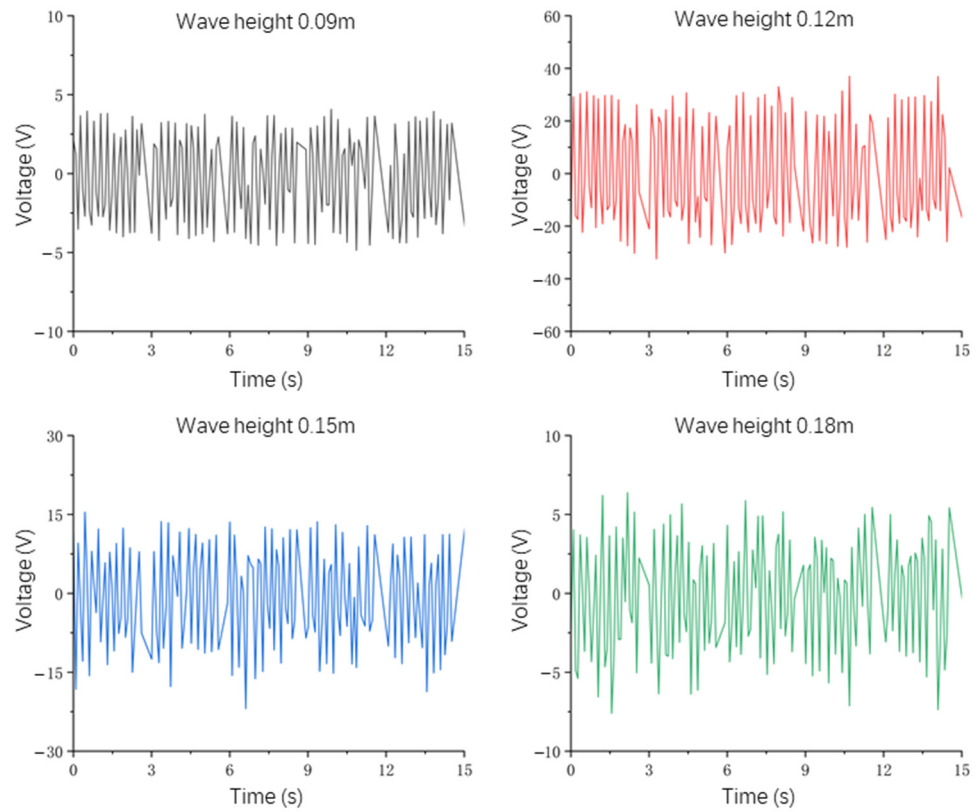


Figure 16. When the wave period is 2.5 s, the open-circuit voltage output of center pipe wave power converter in different significant wave heights.

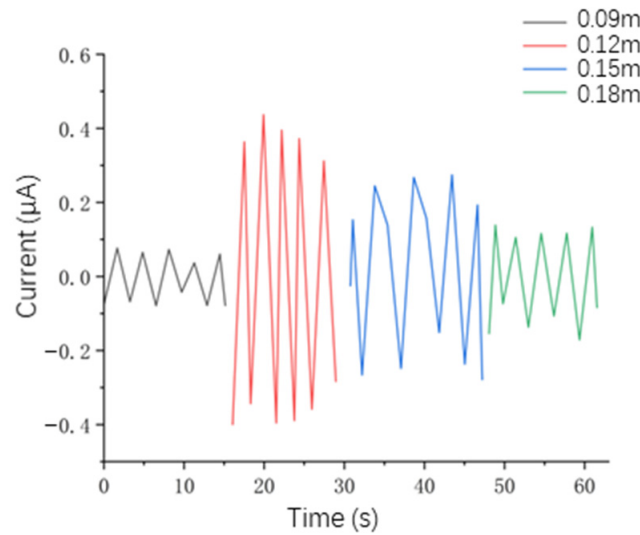


Figure 17. When the wave period is 2.5 s, the short-circuit voltage output of center pipe wave power converter in different significant wave heights.

The electrical performance output of the center pipe wave power generation device at different wave levels when the wave period is 3 s is shown in Figures 18 and 19. It can be seen from the figure that when the significant wave height is 0.12 m, the electrical performance output of the device is the best, the open circuit voltage is about 25 V, and the short-circuit current is about 0.23 μA .

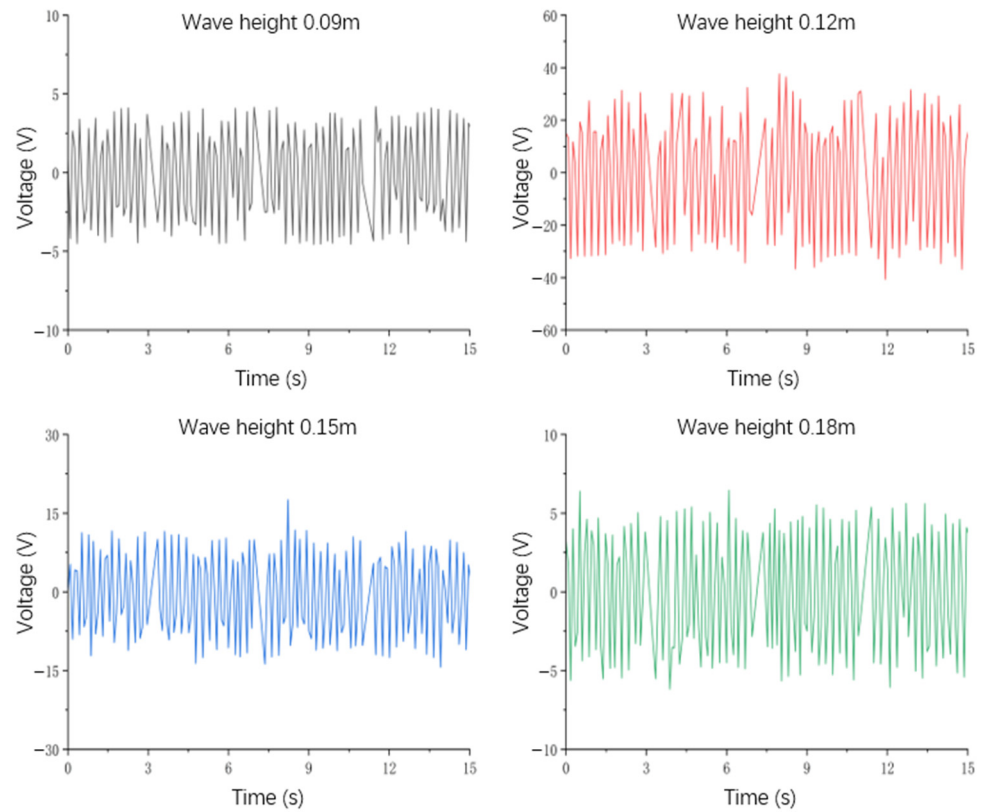


Figure 18. When the wave period is 3 s, the open-circuit voltage output of center pipe wave power converter in different significant wave heights.

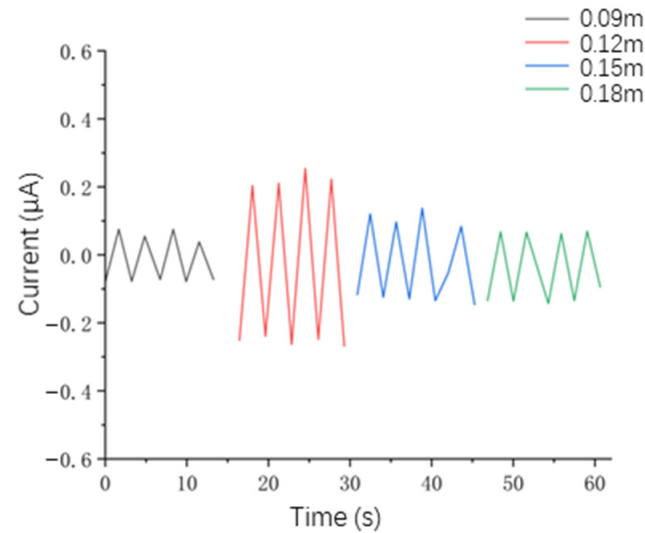


Figure 19. When the wave period is 3 s, the short-circuit voltage output of center pipe wave power converter in different significant wave heights.

The electrical performance output of the center pipe wave power generation device at different wave levels when the wave period is 3.5 s is shown in Figures 20 and 21. It can be seen from the figure that when the significant wave height is 0.12 m, the electrical performance output of the device is the best, the open circuit voltage is about 23 V, and the short-circuit current is about 0.25 μA .

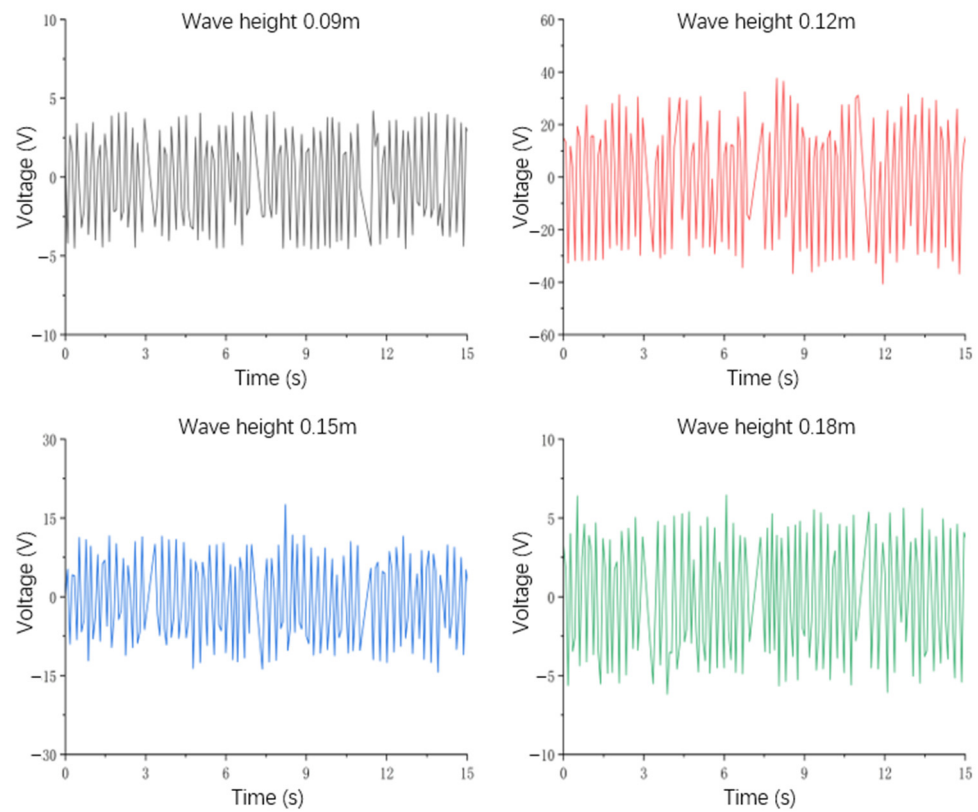


Figure 20. When the wave period is 3.5 s, the open-circuit voltage output of center pipe wave power converter in different significant wave heights.

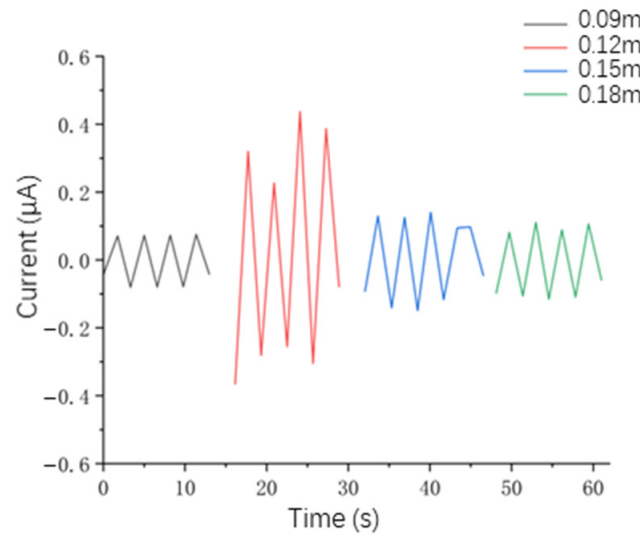


Figure 21. When the wave period is 3.5 s, the short-circuit voltage output of center pipe wave power converter in different significant wave heights.

Four groups of different significant wave heights were tested in the above four different periods. It was found that when the significant wave height was 0.12 m, the electrical performance output of the central pipe-type wave energy triboelectric nanogenerator was the best in the four groups of cycles from 2 to 3.5 s, and the electrical performance output diagram showed that the output characteristics were related to the wave period. Through the test, it can be intuitively observed that when the period is shorter and the significant wave height is higher, the sag and swing of the device are more intense. When the frequency is lower than 2.5 s, the swing of the device is more intense. When the frequency is higher

than 2.5 s, the sag motion of the device is good, and the swing amplitude is not large. Due to the large airflow fluctuation in the pipe, the test turbine's moving blade collides with the guide blade. As the gap between the moving blade and the guide blade increases, the interface gap of the triboelectric nanogenerator enlarges, the motion contact condition is poor, and the electrical performance output is limited by environmental factors, such as humidity.

(2) Electrical performance output under irregular waves

In the irregular wave test, the Jonswap spectrum was adopted, and the effective significant wave height was set to 0.12 m, the Gama value to one, the period to 2.5 s, the wave train length to 1024, and the random seed number to 1000. The measured electrical performance output of the central pipe wave power generator under random wave conditions is shown in Figure 22. It can be seen from the figure that the open circuit voltage is about 5 V, and the short-circuit current is about 0.62 μ A. Compared with the regular wave with the same significant wave height and the same period, the power generation performance exhibits little difference.

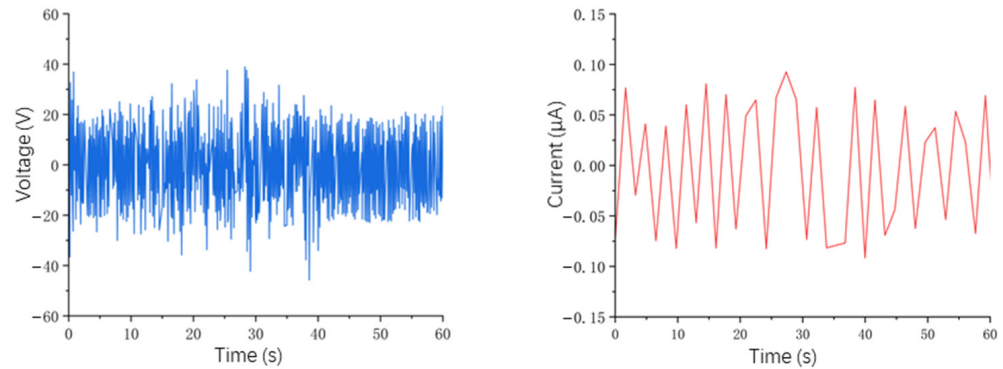


Figure 22. Irregular wave electrical performance output of central pipe wave power generation device with a wave period of 2.5 s.

(3) Small electronic component self-energy application

The charging condition of the 1000 μ F capacitor under a regular significant wave height of 0.12 m and a period of 2.5 s was tested. In the test charges, after 296 s of operation of the central pipe-type wave energy triboelectric nanogenerator, the 1000 μ F capacitor was charged to 1.5 V, and the thermometer with electronic digital display was successfully driven to work, as shown in Figure 23. In the test, 33 LEDs were directly lit on the driven device, as shown in Figure 24.

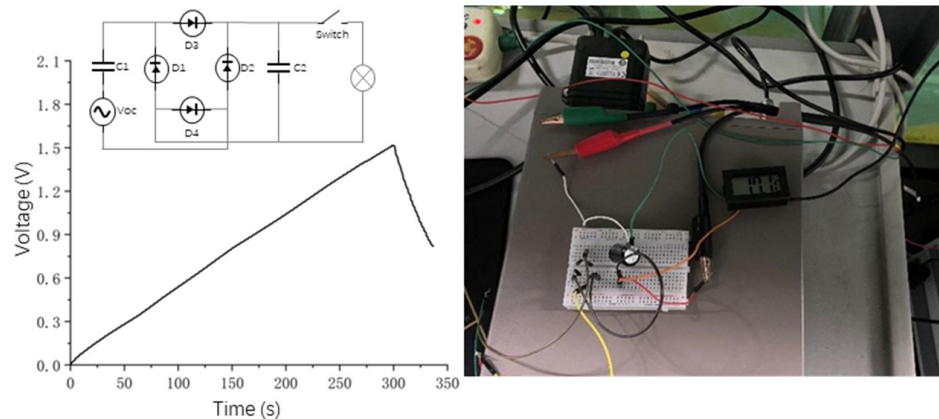


Figure 23. Prototype charged the 1000 μ F capacitor and drove the electronic digital thermometer under the action of a regular wave with a significant wave height of 0.12 m and a period of 2.5 s.



Figure 24. Prototype lights the LED lamp under the action of a regular wave with a height of 0.12 m and a period of 2.5 s.

8. Conclusions

In this paper, both central pipe wave energy capture technology and triboelectric nanogenerator technology were combined to devise a feasible wave energy generation device in terms of miniaturization and performance improvement. The main achievements of this paper include the following:

- (1) A structure combining a central pipe OWC and a triboelectric nanogenerator was designed. The motion equation of the device was established, the working mode of the TENG was preliminarily designed, and its working principle was analyzed.
- (2) Hydrodynamic modeling, a simulation of the structure of the device, and an electrostatic field simulation of the generation mode of the TENG were carried out, and the influence of different parameters on the device were analyzed.
- (3) Optimized design and semi-physical experiments were carried out on the power generation performance parameters of the TENG, through which the effects of dielectric material, thickness, and electrode angle on the power generation performance were identified, and durability experiments were carried out. The results showed that the LED lamp can be successfully lit at a small wave level, verifying the capability of energy supply for small sensors.

In future research, more reasonable assumptions will be applied in the simulation model (such as the compressibility of air in the chamber) and a real sea test will hopefully be carried out to verify the generating efficiency of the proposed OWC. The structure and parameters of the proposed OWC may be further optimized according to the sea test.

Author Contributions: Conceptualization, S.Y.; Methodology, Y.H.; Software, Z.D.; Validation, J.F.; Formal analysis, L.P.; Investigation, Y.T.; Writing—review and editing, B.L. All authors have read and agreed to the published version of the manuscript.

Funding: This work was supported by the following projects: Fujian Provincial Natural Science Youth Funding, China (grant number: 2022J05155). Fujian Provincial Department of Education project (grant number: JAT200248). Xiamen Science and Technology Bureau Nature Funding, China (grant number: 3502Z20227057). Fujian Provincial Department of Science and Technology: University–industry cooperation project, China (grant number: 2023H6016). Fujian Provincial Natural Science funding (grant number: 2023J01791). National Key R&D Program of China (grant number: 2019YFB1504402).

Data Availability Statement: Data are contained within the article.

Conflicts of Interest: The authors declare no conflict of interest.

References

1. Jin, S.; Greaves, D. Wave Energy in the UK: Status Review and Future Perspectives. *Renew. Sustain. Energy Rev.* **2021**, *143*, 110932. [[CrossRef](#)]
2. Silva, J.M.; Vieira, S.M.; Valério, D.; Henriques, J.C.C. GA-Optimized Inverse Fuzzy Model Control of OWC Wave Power Plants. *Renew. Energy* **2023**, *204*, 556–568. [[CrossRef](#)]
3. Drew, B.; Plummer, A.R.; Sahinkaya, M.N. A Review of Wave Energy Converter Technology. *Proc. Inst. Mech. Eng. Part A J. Power Energy* **2009**, *223*, 887–902. [[CrossRef](#)]
4. Yuan, H.; Shaohui, Y.; Hongzhou, H.; Hu, C.; Songgen, Z.; Di, Z. Modeling and Simulation Analysis of Multi-Point Hydraulic Wave Energy Desalination System. *Ocean Eng.* **2019**, *37*, 134–141.
5. Son, D.; Yeung, R.W. Optimizing Ocean-Wave Energy Extraction of a Dual Coaxial-Cylinder WEC Using Nonlinear Model Predictive Control. *Appl. Energy* **2017**, *187*, 746–757. [[CrossRef](#)]
6. Wu, J.; Yao, Y.; Zhou, L.; Göteman, M. Real-Time Latching Control Strategies for the Solo Duck Wave Energy Converter in Irregular Waves. *Appl. Energy* **2018**, *222*, 717–728. [[CrossRef](#)]
7. López, I.; Andreu, J.; Ceballos, S.; Martínez De Alegría, I.; Kortabarria, I. Review of Wave Energy Technologies and the Necessary Power-Equipment. *Renew. Sustain. Energy Rev.* **2013**, *27*, 413–434. [[CrossRef](#)]
8. Ringwood, J.V.; Bacelli, G.; Fusco, F. Energy-Maximizing Control of Wave-Energy Converters: The Development of Control System Technology to Optimize Their Operation. *IEEE Control. Syst.* **2014**, *34*, 30–55. [[CrossRef](#)]
9. Yang, I.; Tezdogan, T.; Incecik, A. Numerical Investigations of a Pivoted Point Absorber Wave Energy Converter Integrated with Breakwater Using CFD. *Ocean Eng.* **2023**, *274*, 114025. [[CrossRef](#)]
10. Sheng, W. Wave Energy Conversion and Hydrodynamics Modelling Technologies: A Review. *Renew. Sustain. Energy Rev.* **2019**, *109*, 482–498. [[CrossRef](#)]
11. Previsic, M.; Karthikeyan, A.; Lyzenga, D. In-Ocean Validation of a Deterministic Sea Wave Prediction (DSWP) System Leveraging X-Band Radar to Enable Optimal Control in Wave Energy Conversion Systems. *Appl. Ocean Res.* **2021**, *114*, 102784. [[CrossRef](#)]
12. Shadman, M.; Guarniz Avalos, G.O.; Estefen, S.F. On the Power Performance of a Wave Energy Converter with a Direct Mechanical Drive Power Take-off System Controlled by Latching. *Renew. Energy* **2021**, *169*, 157–177. [[CrossRef](#)]
13. Russo, S.; Contestabile, P.; Bardazzi, A.; Leone, E.; Iglesias, G.; Tomasicchio, G.R.; Vicinanza, D. Dynamic Loads and Response of a Spar Buoy Wind Turbine with Pitch-Controlled Rotating Blades: An Experimental Study. *Energies* **2021**, *14*, 3598. [[CrossRef](#)]
14. Sheng, W. Motion and Performance of BBDB OWC Wave Energy Converters: I, Hydrodynamics. *Renew. Energy* **2019**, *138*, 106–120. [[CrossRef](#)]
15. Falcão, A.F.O.; Henriques, J.C.C. Oscillating-Water-Column Wave Energy Converters and Air Turbines: A Review. *Renew. Energy* **2016**, *85*, 1391–1424. [[CrossRef](#)]
16. Setoguchi, T.; Takao, M. Current Status of Self Rectifying Air Turbines for Wave Energy Conversion. *Energy Convers. Manag.* **2006**, *47*, 2382–2396. [[CrossRef](#)]
17. Xiao, L.; You, Y.; Zhang, Y. Experimental study on Conical Central Tube Buoy. *Acta Energ. Sin.* **2021**, *42*, 8–14.
18. Li, M.; Chen, T.; Wu, R. Experimental Study On the Influence of the Bottom Shape of Central Tube on the Wave Energy Conversion Performance of Buoy. *New Energy Prog.* **2016**, *4*, 15–19.
19. Wu, B.; Li, M.; Chen, T. An Experimental Study on Energy Conversion of the Modified Centre Pipe Buoy and the Design of Prototypes. *Ocean Eng.* **2017**, *35*, 97–104.
20. Kim, W.D. On the Harmonic Oscillations of a Rigid Body on a Free Surface. *J. Fluid Mech.* **1965**, *21*, 427–451. [[CrossRef](#)]
21. Wang, Z.L. On Maxwell's Displacement Current for Energy and Sensors: The Origin of Nanogenerators. *Mater. Today* **2017**, *20*, 74–82. [[CrossRef](#)]
22. Lin, Z.H.; Cheng, G.; Lin, L.; Lee, S.; Wang, Z.L. Water-Solid Surface Contact Electrification and Its Use for Harvesting Liquid-Wave Energy. *Angew. Chemie—Int. Ed.* **2013**, *52*, 12545–12549. [[CrossRef](#)] [[PubMed](#)]
23. Xu, M.; Wang, S.; Zhang, S.L.; Ding, W.; Kien, P.T.; Wang, C.; Li, Z.; Pan, X.; Wang, Z.L. A Highly-Sensitive Wave Sensor Based on Liquid-Solid Interfacing Triboelectric Nanogenerator for Smart Marine Equipment. *Nano Energy* **2019**, *57*, 574–580. [[CrossRef](#)]
24. Yang, Y.; Zhang, H.; Liu, R.; Wen, X.; Hou, T.C.; Wang, Z.L. Fully Enclosed Triboelectric Nanogenerators for Applications in Water and Harsh Environments. *Adv. Energy Mater.* **2013**, *3*, 1563–1568. [[CrossRef](#)]
25. Wang, N.; Zou, J.; Yang, Y.; Li, X.; Guo, Y.; Jiang, C.; Jia, X.; Cao, X. Kelp-Inspired Biomimetic Triboelectric Nanogenerator Boosts Wave Energy Harvesting. *Nano Energy* **2019**, *55*, 541–547. [[CrossRef](#)]
26. Sarmento, A.J.N.A.; De Falcão, A.F.O. Wave Generation by an Oscillating Surface-Pressure and Its Application in Wave-Energy Extraction. *J. Fluid Mech.* **1985**, *150*, 467–485. [[CrossRef](#)]
27. Falcão, A.F.O.; Henriques, J.C.C. Model-Prototype Similarity of Oscillating-Water-Column Wave Energy Converters. *Int. J. Mar. Energy* **2014**, *6*, 18–34. [[CrossRef](#)]
28. Mazzaretto, O.M.; Menéndez, M.; Lobeto, H. A Global Evaluation of the JONSWAP Spectra Suitability on Coastal Areas. *Ocean Eng.* **2022**, *266*, 112756. [[CrossRef](#)]

Disclaimer/Publisher's Note: The statements, opinions and data contained in all publications are solely those of the individual author(s) and contributor(s) and not of MDPI and/or the editor(s). MDPI and/or the editor(s) disclaim responsibility for any injury to people or property resulting from any ideas, methods, instructions or products referred to in the content.